Detecting nitrogen-vacancy-hydrogen centers on the nanoscale using nitrogen-vacancy centers in diamond

Christoph Findler,[1,2,*] Rémi Blinder,[1] Karolina Schüle,[1] Priyadharshini Balasubramanian,[1] Christian Osterkamp,[2,1] and Fedor Jelezko[1]

[1]*Institute for Quantum Optics, Ulm University, Albert-Einstein-Allee 11, D-89081 Ulm, Germany*

[2]*Diatope GmbH, Buchenweg 23, D-88444 Ummendorf, Germany*

(Received 8 November 2023; accepted 30 January 2024; published 28 February 2024)

In diamond, nitrogen defects like the substitutional nitrogen defect (N_s) or the nitrogen-vacancy-hydrogen complex (NVH) outnumber the nitrogen-vacancy (NV) defect by at least one order of magnitude creating a dense spin bath. While neutral N_s has an impact on the coherence of the NV spin state, the atomic structure of NVH reminds of a NV center decorated with a hydrogen atom. As a consequence, the formation of NVH centers could compete with that of NV centers possibly lowering the N-to-NV conversion efficiency in diamond grown with hydrogen-plasma-assisted chemical vapor deposition (CVD). Therefore, monitoring and controlling the spin bath is essential to produce and understand engineered diamond material with high NV concentrations for quantum applications. While the incorporation of N_s in diamond has been investigated on the nano- and mesoscale for years, studies concerning the influence of CVD parameters and the crystal orientation on the NVH formation have been restricted to bulk N-doped diamond providing high-enough spin numbers for electron paramagnetic resonance and optical absorption spectroscopy techniques. Here, we investigate submicron-thick (100)-diamond layers with nitrogen contents of (13.8 ± 1.6) ppm and (16.7 ± 3.6) ppm, and exploiting the NV centers in the layers as local nanosensors, we demonstrate the detection of NVH^- centers using double electron-electron resonance (DEER). To determine the NVH^- densities, we quantitatively fit the hyperfine structure of NVH^- and confirm the results with the DEER method usually used for determining N_s^0 densities. With our experiments, we access the spin bath composition on the nanoscale and enable a fast feedback loop in CVD recipe optimization with thin diamond layers instead of resource- and time-intensive bulk crystals. Furthermore, the quantification of NVH^- plays a very important role for understanding the dynamics of vacancies and the incorporation of hydrogen into CVD diamond optimized for quantum technologies.

DOI: 10.1103/PhysRevMaterials.8.026203

I. INTRODUCTION

Solid-state quantum systems based on point defects in crystals like silicon carbide and diamond are promising platforms for quantum technologies since they can host fluorescent electron spin defects with long coherence times [1–3]. Typical defect concentrations range from parts per trillion (ppt) for single and isolated centers to dense ensembles with several parts per million (ppm) defects in the host material. As a consequence, analyzing these defects and their local environment is challenging, in particular for ultrapure crystals. In case of fluorescent defects, confocal microscopy is capable of resolving single atomic defects, like, for instance, the negatively charged nitrogen-vacancy center (NV^-) in diamond [4]. The defect consists of a substitutional nitrogen, an adjacent carbon vacancy and an electron from a donor [Fig. 1(a)]. Its electron spin ($S = 1$) exhibits coherence times up to several milliseconds [2,5] and it can be controlled by laser and microwave pulses [4]. Its atomic size and the high sensitivity to magnetic fields [6,7] makes the NV^- an ideal sensor for nuclear magnetic resonance spectroscopy in nano- [8–10] and micron-sized volumes [11,12]. Likewise, the sensing characteristics of the NV^- center can also be exploited to analyze the density and nature of electron spins [13] that usually form when doping diamond with nitrogen [14].

Hydrogen-plasma-assisted chemical-vapor deposition (CVD) of diamond represents currently the state-of-the-art method to synthesize N-doped diamond for NV^- applications with adjustable thickness [15–17] and concentration [18–20]. Despite the progress in engineering CVD-grown diamond, low N-to-NV conversion efficiencies of a few percent or less [14,19–22] remain still a problem. In other words, the CVD recipes of today produce mostly other nitrogen-related defects than NV^-.

In (100)-oriented diamond, for example, substitutional nitrogen (N_s) can be up to 300 times more abundant than NV^- [14]. Substitutional nitrogen in its neutral charge state (N_s^0 or P1) is a paramagnetic but nonfluorescent (dark) defect carrying a $S = 1/2$ spin [23] and, hence, constitutes a spin

*christoph.findler@uni-ulm.de

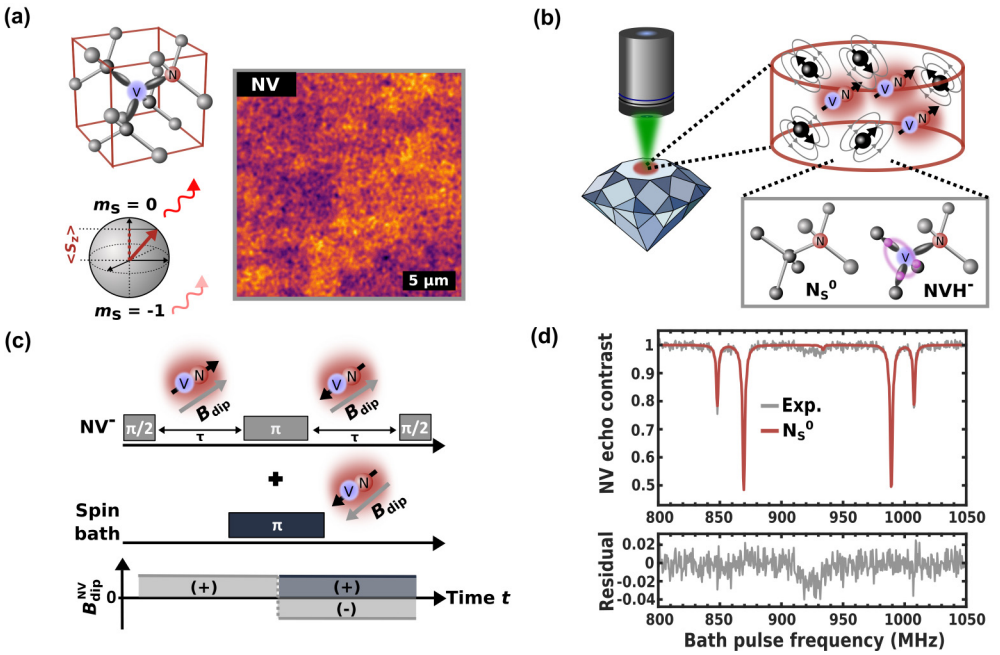

FIG. 1. (a) The structure of the NV-center in diamond and a confocal microscopy image of sample A. The Bloch-sphere illustrates the spin-dependent fluorescence that is exploited for spin-state readout. (b) Confocal microscopy analysis of a NV^- ensemble and the local paramagnetic spin bath consisting of substitutional nitrogen (N_s^0) and the negatively charged nitrogen-vacancy-hydrogen complex (NVH^-). The quasistatic magnetic field is measured through the NV^- ensemble (c) Double electron-electron resonance (DEER) pulse sequence for probing the quasistatic, dipolar magnetic field B_{dip} of paramagnetic spins using NV^- centers as local sensors. (d) Experimental DEER spectrum for sample A at 330 G aligned along ⟨111⟩ including a fit with a $^{15}N_s^0$-spin model. The bath π pulse is 525 ns long and $\tau = 1.5$ µs.

bath around the NV^- centers [Fig. 1(b)] often limiting their coherence time T_2 [24]. As a consequence, a high NV^-:N_s^0 ratio is favorable for sensing applications as it results in reduced magnetic noise, i.e., enhanced coherence time, and an increased number of interrogated NV^- centers, potentially leading to higher signal-to-noise ratio [25].

One way for increasing the NV^- concentration in CVD diamond is generating additional vacancies by electron irradiation and converting them together with N_s^0 by annealing into NV^- [20,26]. Other studies optimize the CVD process itself by varying the substrate orientation [19,22], the nitrogen source [21], the N:C ratio in the gas phase [19,26], or the growth temperature [22,27]. In particular, changing from the growth on (100)- to (113)-oriented substrates and optimizing the growth temperature has been reported to yield NV^-:N_s^0 ratios of up to 25% without any posttreatment [22]. The origin of the improvement remains unclear and a better understanding of the generation of defects in CVD-grown diamond is thus crucial.

The second most abundant spin species in CVD diamond [14], the negatively charged nitrogen-vacancy-hydrogen defect (NVH^-), structurally reminds of a NV center decorated with an additional hydrogen atom [28] [Fig. 1(b)]. The latter undergoes fast tunneling between the carbons adjacent to the defect's vacancy causing an effective [111]-oriented C_{3v} symmetry [28,29]. However, NVH^- has a different spin multiplicity ($S = 1/2$) and different optical properties compared to the NV center. In particular, to our knowledge there is no reported fluorescence for NVH^-. As a consequence, being usually one order of magnitude more abundant than NV^- in (100)-oriented CVD diamond [14,20], the nonfluorescent NVH defect comes under suspicion to reduce the N-to-NV conversion degree. The formation mechanism of NVH remains still unknown, though. One possibility is the incorporation as whole units [14] and/or NV centers get passivated after their formation by H atoms [14,30,31]. Either way, NVH centers have to be considered as a possible sink for NV centers, which is why their density should be studied carefully and their generation understood to develop superior diamond growth.

The main technique to investigate paramagnetic spins is electron paramagnetic resonance (EPR) spectroscopy [32]. For bulk single-crystalline diamond with a sample volume of a few mm^3, conventional EPR spectrometers are sensitive to defect concentrations down to parts per billion (ppb) [14]. This capability has proven useful in several cases of in-depth studies on bulk diamond material [14,20,26] or defect dynamics induced by thermal annealing [33–35]. However, for quantum applications on the nano/mesoscale like nuclear magnetic resonance spectroscopy [8,11,12] or wide-field magnetometry of substances outside of the diamond [36–40], single centers or thin NV^- layers with thicknesses of a few microns close to the surface are required. As a result, the number of spins involved lies several orders of magnitude below the sensitivity of conventional EPR. Likewise, techniques based on absorption spectroscopy (IR or UV visible) [21,41] show equivalent sensitivity limits for thin layers.

Optically detected double electron-electron resonance (DEER) using NV^- centers as local magnetic field sensors, on the other hand, works even with single atomic centers [42]

and the technique has already been applied to investigate N_s^0 in nm-thin layers [16,19,22,43]. In this paper, we demonstrate that DEER is also capable of detecting NVH^-, even for densities of only a few hundreds of ppb. The defect nature is confirmed by resolving the hyperfine structure expected for NVH^- and we determine the bath density by quantitatively fitting DEER spectra of submicron-thick layers considering multiple spin species and forbidden transitions. Finally, the obtained NVH^- concentrations are verified by following a well-established DEER approach for estimating N_s^0 bath densities [13,16,19,22].

II. RESULTS AND DISCUSSION

For detecting NVH^- in thin diamond layers, we prepare two ^{15}N-doped samples with slightly different nitrogen concentrations as determined by secondary ion-mass spectrometry (SIMS), i.e., (13.8 ± 1.6) ppm for sample A and (16.7 ± 3.6) ppm for sample B. According to SIMS, the thicknesses of the N-doped layers are respectively (570 ± 60) nm and (700 ± 50) nm for sample A and B. Both layers are homoepitaxially grown on (100)-oriented single-crystalline substrates using microwave-assisted plasma chemical vapor deposition (CVD) with ^{12}C-enriched (99.99%) methane and $^{15}N_2$ (98%) gas. The details of the CVD process are provided in the Supplemental Material (SM) [44].

Utilizing a confocal microscope, we probe the fluorescence of NV^- centers by optical excitation with a green laser. By scanning the laser over the diamond we obtain a confocal microscopy image as shown in Fig. 1(a) (sample A). Following the procedure reported by Osterkamp *et al.* [45], we estimate the NV^- concentration based on photon emission averaged over a confocal scan like shown in Fig. 1(a) and calibrating the method with the emission of a single NV^- center under identical experimental conditions. As a result, we find approximately 12 ppb and 16 ppb for sample A and B, respectively. In total we investigate three NV^- ensembles per diamond sample labeled A1,2,3 and B1,2,3, respectively. For the coherence time T_2 measured by a Hahn-Echo, we obtain 15 µs for sample A and 10 µs for sample B. The analysis of the dark spin environment is first demonstrated using ensemble A1 and B1 as an example and later extended to the remaining ensembles.

Considering the thickness of the doped layers and the dimensions of our confocal volume [300 x 300 x 500 nm^3 (FWHM)], the layers studied in this paper are completely illuminated by the laser and lie entirely in the confocal volume with respect to depth, i.e., can be considered as optically two dimensional. With microwave pulses we control the spin state of the NV^- centers in the interrogated volume by magnetic resonance. Dark, paramagnetic defects like N_s^0 and NVH^-, can also be addressed by microwaves but, due to the lack of spin-dependent fluorescence, no direct optical readout of their spin state has been reported at room temperature. The defect N_s^0, however, causes a quasistatic magnetic field that can be sensed by NV^- centers scattered around [Fig. 1(b)] [13,16]. Therefore, one can exploit the dipolar coupling between the fluorescent NV^- centers and the dark spins to estimate the density of the latter ones [13,16,19]. For this we employ optically detected three-pulse DEER [13,16] where the first pulses on NV^- $(\pi/2 - \pi)$ correspond to the usual Hahn echo, and the last $\pi/2$ converts the magnetization from the equatorial plane to the z direction for optical readout [Fig. 1(c)]. Without any π pulse on the bath, the Hahn echo decouples the NV^- ensemble from the quasistatic, local magnetic field created by the bath spins B_{dip} [13,16]. The corresponding phase accumulated for the NV^--spin state on the Bloch sphere during the Hahn echo sequence reads at the time $t = 2\tau$ as $\varphi_{2\tau} = \int_{t=0}^{2\tau} B_{\mathrm{dip}}^{\mathrm{NV}} dt$, with $B_{\mathrm{dip}}^{\mathrm{NV}} = (B_{\mathrm{dip}}, -B_{\mathrm{dip}})$ in the first $(t < \tau)$ and second part of the sequence respectively. Consequently, the phases accumulated in the two segments, $[0, \tau]$ and $[\tau, 2\tau]$, of the Hahn echo cancel each other [Fig. 1(c)]. Adding the resonant bath π pulse, however, leads to the simultaneous inversion of B_{dip} with the NV^- spin state resulting in a nonzero phase $\varphi_{2\tau} = \int_{t=0}^{2\tau} B_{\mathrm{dip}}^{\mathrm{NV}} dt \neq 0$, which translates into decoherence [Fig. 1(c)]. The coherence left after recoupling B_{dip} of a spin bath with the density n_{bath} to the NV^- ensemble is called DEER intensity and can be written as [13,16]

$$C_{\mathrm{DEER}} = C_\tau \exp\left(-A\gamma_{\mathrm{NV}}\gamma\, n_{\mathrm{bath}} T \left\langle \sin^2\left(\frac{\theta}{2}\right)\right\rangle_L\right), \quad (1)$$

with $C_\tau = C_0 \exp(-2\tau/T_2)$, $A = 2\pi\mu_0\hbar/9\sqrt{3}$, T as the timing of the bath π pulse relative to the NV^- $\pi/2$ pulse [Fig. 3(b) below], and $\gamma_{\mathrm{NV}} = g_{\mathrm{NV}}\mu_B/\hbar$, $\gamma = g\mu_B/\hbar$ as the gyromagnetic ratios for NV^- and the bath spins, respectively. The constant $\hbar$ is the reduced Plank constant, μ_0 the vacuum permeability, μ_B the Bohr magneton, g_{NV} and g are the g factors of the NV^- centers and the bath spins, respectively. The factor C_0 in C_τ represents the maximal contrast obtained from the NV^- centers and the term $\exp(-2\tau/T_2)$ accounts for the loss of coherence during the DEER sequence $(t = 2\tau)$ that is not related to the partial inversion of the bath spins. The parameter θ is the flip angle induced by the pulse on the bath spins [13]. It is worth remarking that $\sin^2(\theta/2)$ in Eq. (1) corresponds to the probability of spin inversion by the applied π pulse. Thus, for a dark spin ensemble, the sine term in Eq. (1) represents the fraction of spins that are successfully inverted. In the ideal case $(\theta = \pi)$ the inverted fraction is 1. Practically, however, proper inversion is attained only for spin species that are well on resonance with the pulse carrier frequency. To consider the actual distribution of flip angles across the dark spins, averaging of $\sin^2(\theta/2)$ needs to be performed over the full, inhomogeneously broadened spectrum denoted by the brackets $\langle\rangle_L$ in Eq. (1).

For the DEER spectrum measured for NV^- ensemble A1 in Fig. 1(d), we fix $T \sim \tau$ in the Hahn echo and vary the frequency of the bath π pulse around the transition frequency of a free $S = 1/2$ electron spin in a static, external magnetic field $B_0 = 330$ G, here $\nu_{\mathrm{free}} = 924$ MHz. Subtracting the DEER intensity obtained with a $3\pi/2$ pulse before the optical readout in Fig. 1(c) from the results with a $\pi/2$ pulse instead yields the NV echo contrast shown in Fig. 1(d). We observe four major and one broad, small signals around ν_{free} in the DEER spectrum [Fig. 1(d)]. Since $^{15}N_s^0$ is expected to be the most abundant paramagnetic defect in ^{15}N-doped diamond [13,14,16,19], we fit Eq. (1) to the experimental data in [Fig. 1(d)] using the MATLAB toolbox Easyspin [46], the actual duration of the bath π pulse, and the spin Hamiltonian for $^{15}N_s^0$, $\hat{H} = g\mu_B\vec{B}_0\hat{S} + \hat{S}\overleftrightarrow{A}\hat{I}$ [23] with $S = 1/2$ [23],

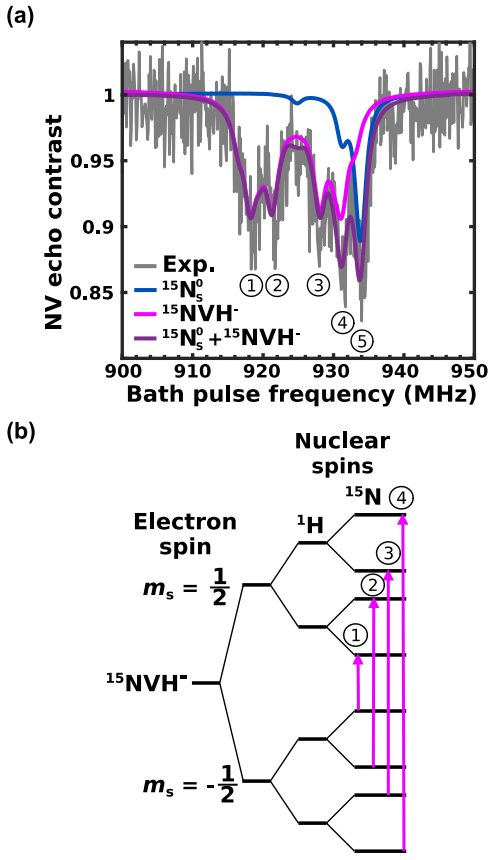

FIG. 2. (a) High resolution DEER spectrum acquired at 330 G aligned along ⟨111⟩ and π pulse length of 975 ns using $\tau = 10\,\mu$s. The numbers 1 – 5 label the most prominent resonances in the spectrum and are assigned to the spin transitions represented by pink arrows in (b). (b) Level scheme of the $S = 1/2$ electron spin of ^{15}NVH$^-$. The spin states $m_S = \pm 1/2$ get split each into four sublevels due to hyperfine interaction with ^{1}H and ^{15}N.

$g = 2.0024$ [23], $I = 1/2$ [23], $A_\parallel$ = -159.73 MHz [23], and $A_\perp$ = –113.84 MHz [23] to calculate $\langle \sin^2(\theta/2)\rangle_L$ by numerical evaluation of the pulse propagator, as described in the SM [44]. The numerical approach is an extension to the analysis of the DEER intensity reported in Stepanov *et al.* [13] as we are able to consider forbidden transitions and simultaneous driving of multiple transitions in our refinement. Examining the vanishing residual around the four major dips in Fig. 1(d) confirms $^{15}N_s^0$ to mostly constitute the spin bath in sample A, an observation that is also valid for sample B with the higher nitrogen concentration (see the SM [44]). Using that for a $^{15}N_s^0$ bath ($S = 1/2$ and $g = 2.0024$ [23]) the factor $A\gamma_{\rm NV}\gamma$ in Eq. (1) becomes 0.292 MHz/ppm [13,16], we extract the $^{15}N_s^0$ concentrations given in Table I from the quantitative fit with Eq. (1), as shown for sample A in Fig. 1(d).

By contrast, examining the spectrum in Fig. 1(d) between 900 and 950 MHz, we find a significant residual comparing model and experiment. Although considering a forbidden $^{15}N_s^0$ transition around 930 MHz, the signal observed between 910 MHz and 930 MHz seems not be explained by $^{15}N_s^0$ only. Interestingly, the same spectrum is also observed for sample B, cf. SM [44]. To further investigate the DEER intensity between 900 MHz and 950 MHz,

TABLE I. The concentrations of $^{15}N_s^0$ and ^{15}NVH$^-$ obtained from fitting the DEER spectrum (spec.) and the π-shift method (π). For $^{15}N_s^0$, the allowed transitions as for example in Fig. 1(d) are fitted while for ^{15}NVH$^-$ only the region between 900 MHz and 950 MHz is used [Fig. 2(a)]. The full set of fit parameters are provided in the SM [44] . In case of the π-shift method for $^{15}N_s^0$ the experiments are performed on each resonance line [cf. Fig. 1(d)] and the results summed up. For ^{15}NVH$^-$, the experimental data from a single π-shift experiment is fitted using Eq. (2) with the calculated fractions of inverted spins $x_{N_s^0}$, $x_{\rm NVH^-}$ [Fig. 3(a)].

Ensemble	$n_{N_s^0}$ (ppm)	$n_{\rm NVH^-}$ (ppm)	$x_{N_s^0}$	$x_{\rm NVH^-}$
A1 (spec.)	7.66 ± 0.12	0.40 ± 0.02		
A1 (π)	6.65 ± 0.55	0.34 ± 0.07	0.007	0.448
B1 (spec.)	11.02 ± 0.28	0.81 ± 0.04		
B1 (π)	9.90 ± 0.87	0.67 ± 0.14	0.004	0.597

we reduce the microwave power that the bath π pulse is two-times longer than in Fig. 1(d), i.e., 975 ns and 525 ns, respectively. By this, we address the bath spins more precisely with limited power broadening and find at least five resonances (1-5) [Fig. 2(a)], where peak no. 5 corresponds to the forbidden transition of $^{15}N_s^0$ already evident in Fig. 1(d). The remaining peaks, no. 1–4, seem to arise from another spin species and, therefore, we extend our model by adding the usually second most-abundant spin in ^{15}N-doped diamond [14], i.e., ^{15}NVH$^-$, with the Hamiltonian $\hat{H}_{^{15}\rm NVH} = g\mu_B\vec{B}_0\hat{S} + \hat{S}\overleftrightarrow{A}_{^{15}\rm N}\hat{I}_{^{15}\rm N} + \hat{S}\overleftrightarrow{A}_{^1\rm H}\hat{I}_{^1\rm H}$ where $A_{\parallel,15N} = 2.9$ MHz [28], $A_{\perp,15N} = 3.1$ MHz [28], $A_{\parallel,1H} = 13.69$ MHz [28], $A_{\perp,1H} = -9.05$ MHz [28]. Assuming two randomly distributed spin species of concentrations n_1 and n_2, Eq. (1) extends then to

$$C_{\rm DEER} = C_\tau \exp\left(-A\gamma_{\rm NV}\gamma T[n_1x_1 + n_2x_2]\right), \qquad (2)$$

where $x_1 = \langle \sin^2(\theta/2)\rangle_{1,L}$ and $x_2 = \langle \sin^2(\theta/2)\rangle_{2,L}$ are the inverted fractions for spin species 1 and 2. We have made the approximation that both species have an isotropic and equal g factor and therefore have the same gyromagnetic ratio $\gamma = g\mu_B/\hbar$. Indeed, taking species 1 as $^{15}N_s^0$ and species 2 as ^{15}NVH$^-$, one obtains $|g_2/g_1 - 1| < |2.0034/2.0024 - 1| = 5.0e-4 \ll 1$, which validates the approximation.

Including also ^{15}NVH$^-$ into the model, the fit agrees well with the experimental data in Fig. 2(a) and, therefore, we attribute the signal observed between 910 MHz and 930 MHz to ^{15}NVH$^-$ spins in our doped layer. The resonances no. 1–4 are well reproduced by the model, and thus can be assigned to the identically labeled electron spin transitions in Fig. 2(b). Since the ^{15}NVH$^-$ center hosts two nuclear spins (^{15}N and ^{1}H) each with $I = 1/2$, the two electron spin states $m_S = \pm 1/2$ split up each into four hyperfine states leading to four transitions, represented by pink arrows in Fig. 2(b). The major resonances, 1–4 in Fig. 2(a), correspond to the three equivalent orientations of ^{15}NVH$^-$ centers that are not aligned with $\vec{B}_0$. Since the effective hyperfine interaction between the electron and the nuclear spin (^{15}N or ^{1}H) depends on the orientation of the defect with respect to the magnetic field, the transition frequencies differ for the aligned and the not-aligned ^{15}NVH$^-$ centers. In particular, the aligned subset

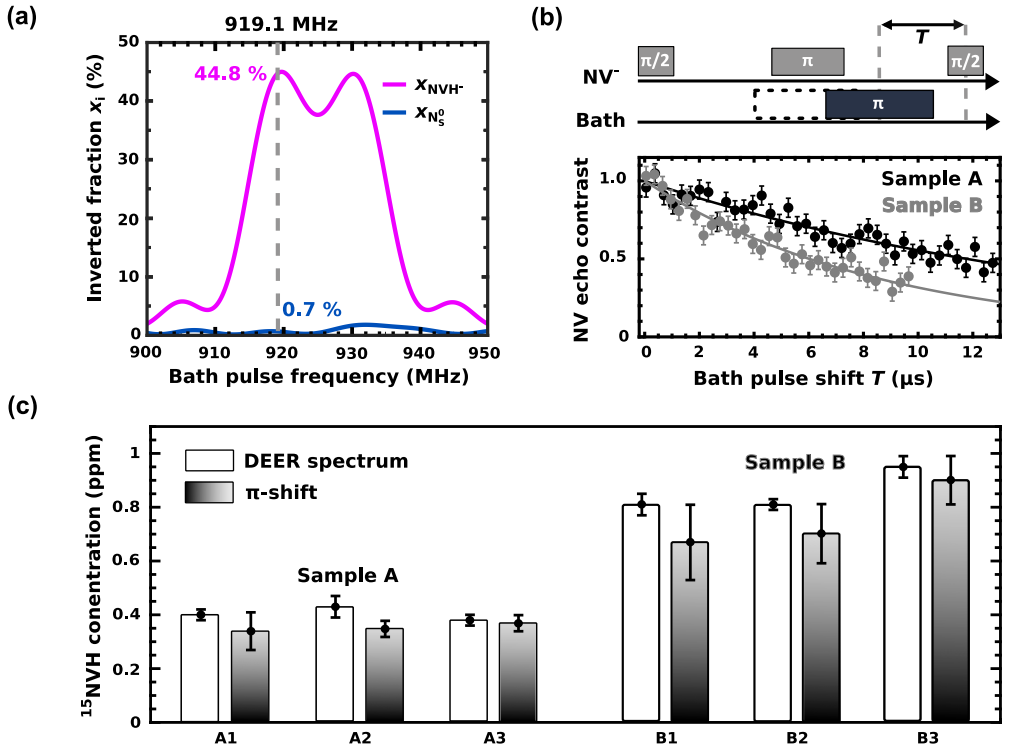

FIG. 3. (a) The fraction of spins inverted by a 93.4 ns π pulse as a function of the pump frequency for ensemble A1. The calculation is performed with EasySpin using the linewidths and experimental parameters obtained from the fit in Fig. 2(a). (b) Pulse sequence of the π-shift method and experimental results for ensembles A1 and B1. The solid lines correspond to fits with monoexponentials defined by Eq. (2). (c) Comparison of the ^{15}NVH$^-$ concentrations obtained from the quantitative fit method for the high resolution spectra [Fig. 2(a)] and the π-shift method [see (b)] for six NV ensembles in sample A and B. The uncertainties correspond to fit errors (95% confidence interval).

experiences slightly larger ^{1}H splittings, causing weak shoulders in Fig. 2(a). Additional forbidden transitions contribute to the intensity in the central region around 925 MHz but cannot be individually resolved. By repeating the measurements and the fitting procedure with Eq. (2) for sample B we observe the same hyperfine structure (see the SM [44]) and Table I summarizes the obtained ^{15}NVH$^-$ concentrations for ensemble A1 and B1. The higher ^{15}NVH$^-$ concentration in sample B can be attributed to the overall higher nitrogen concentration in sample B than in A. As a consequence, the more dense spin bath in sample B explains also the broader Lorentzian linewidth for ^{15}NVH$^-$ spins, with (2.44 ± 0.18) MHz and (1.33 ± 0.11) MHz (FWHM) for ensemble B1 and A1, respectively. It should be noted that the linewidths given above are not affected by power broadening since the effect of the microwave power is considered in the model separately from intrinsic inhomogeneous broadening (see the SM [44]).

So far, we have demonstrated that ^{15}NVH$^-$ can be detected in submicron thick ^{15}N-doped diamond layers using optically detected DEER with NV$^-$ as atomic-sized sensors. The presented method, however, is also applicable to detect ^{14}NVH$^-$ in ^{14}N-doped diamond. Studying a sample grown with identical parameters as sample A but using ^{14}N as dopant, yields the DEER spectra in the SM [44]. Due to the $I = 1$ nuclear spin of ^{14}N we observe an additional allowed transition arising from ^{14}N$_s^0$ that overlaps with half of the ^{14}NVH$^-$ spectrum [28]. Using the quantitative fitting method with Eq. (2) and the hyperfine tensor derived from ^{15}NVH$^-$ [28], confirms successfully the measured DEER signal to arise from ^{14}NVH$^-$.

An alternative method for determining the spin bath concentrations is shifting the resonant bath π pulse by T with respect to one of the NV$^-$ $\pi/2$ pulses [Fig. 3(b)]. The NV-echo contrast C_{DEER} follows then a monoexponential decay given by Eq. (1) or (2), for the case of one or two bath spin species, respectively. For the allowed transitions of ^{15}N$_s^0$, the spectral overlap with ^{15}NVH$^-$ is negligible [Fig. 1(d)], so that Eq. (1) can be used. This technique has been used in several studies to analyze the N$_s^0$ bath in diamond layers [16,19,22,47] and we here refer to it as π-shift method. Performing the π-shift method on each N$_s^0$ transition frequency and fitting Eq. (1) to the experimental data in the SM [44], we extract a total ^{15}N$_s^0$ bath concentration of (6.7 ± 0.6) ppm and (9.9 ± 0.9) ppm, for sample A and B, respectively (Table S9 within the SM [44]). The N$_s^0$ concentrations obtained from the quantitative fits of the spectra in Table I agree well with the results from the π-shift method.

As a result, one should be able to estimate the ^{15}NVH$^-$ concentration in the same way. However, unlike for N$_s^0$, the ^{15}NVH$^-$ resonances lie spectrally very close together and overlap with the forbidden transitions of ^{15}N$_s^0$ [Fig. 2(a)]. Additionally, the expected concentration of NVH$^-$ is smaller by one order of magnitude than that of ^{15}N$_s^0$ (Table I). Hence, we apply a π pulse with a duration of 93 ns and frequency of

919.1 MHz that we drive simultaneously transition no. 1 and 2 in Fig. 2(a) to enhance the DEER contrast from ^{15}NVH$^-$ spins. Figure 3(a) shows the calculated inverted fractions $x_{N_s^0}$ and x_{NVH^-} in Eq. (2) applying a 93-ns long π pulse depending on the bath pump frequency. For the calculation of x_i we use in EasySpin the linewidths obtained from the fit in Fig. 2(a) for ensemble A1. Due to the strong π pulse in Fig. 3(a), transition no. 1 and 2 merge to one peak and applying the π pulse with 919.1 MHz results in a spin inversion of 44.8% and 0.7% for ^{15}NVH$^-$ and $^{15}N_s^0$, respectively. Varying the pulse timing T, the NV echo contrast in Fig. 3(b) follows a monoexponential decay that is fitted with Eq. (2). For the $^{15}N_s^0$ concentration we use the value from the π-shift method (Table I) and obtain for ^{15}NVH$^-$ (0.34 ± 0.07) ppm. Comparing with the concentration, (0.40 ± 0.02) ppm, previously obtained from the quantitative fit of the spectrum in Fig. 2(a), it can be seen that both methods agree with each other. Our results demonstrate that the π-shift method is applicable also in the case of overlapping resonances of two species, provided the concentration of one of them has been separately determined. Repeating the analysis for sample B with the higher nitrogen content, we observe a faster decay than for sample A in Fig. 3(b) resulting after analysis in a significant higher ^{15}NVH$^-$ concentration of (0.67 ± 0.14) ppm. As for sample A, the result agrees well with the (0.81 ± 0.04) ppm from the quantitative fit of the DEER spectrum. Repeating the spin bath analysis for the NV ensembles A2,3 and B2,3 yields within one method consistent ^{15}NVH$^-$ concentrations for sample A and B. Comparing the results of both approaches, however, we find systematically higher values for the DEER spectrum than for the π-shift method [Fig. 3(c)].

The main difference between the spectrum and the π-shift method is the applied microwave power to excite the spin bath. In case of ensemble A1, for instance, using a ten-times shorter π pulse for acquiring the signal in Fig. 3(b) (93 ns) than for the spectrum in Fig. 2(a) (975 ns), the contribution to the DEER intensity from off-resonant driving of allowed $^{15}N_s^0$ transitions is expected to be bigger for the π-shift method than for the DEER spectrum. In Fig. 3(a) we consider the nonresonant excitation of $^{15}N_s^0$ spins, but we assume rectangular-like π pulses for calculating $x_i = \langle \sin^2(\theta_i/2) \rangle_L$ in EasySpin. As in the experiment the pulse shape can deviate from our assumption, the calculated inverted spin fractions might be not exact for high microwave powers leading to a possible overestimation of the contribution from $^{15}N_s^0$ to the DEER intensity in Fig. 3(b). But considering the small difference between the concentrations from the spectrum and the π-shift method in Fig. 3(c), the assumption of rectangular-like pulses seems to be a reasonable approximation for determining the ^{15}NVH$^-$ concentration with a short, high power microwave pulse in Figs. 3(a) and 3(b). In fact, a higher microwave power results in a stronger NV echo contrast and, therefore, shorter data acquisition time. The DEER spectrum for sample A in Fig. 2(a), for example, has been measured for more than one day while the π-shift method like in Fig. 3(b) takes only a few hours. Once the typical linewidth of the NVH$^-$ spins in a given sample is determined, the inverted fractions can be calculated, and one could rely on the π-shift method only to analyze the spin bath around various NV$^-$ ensembles in an time-efficient way. This works under the assumption that large variations of the spin concentration can be excluded as this might influence the linewidths. For heterogeneous diamond layers, one should stick to the quantitative fit of the DEER spectrum as it considers directly the linewidths of the spin species and is therefore more robust.

For samples with defect concentrations lower than in the present study, the pulse spacing τ in Fig. 1(c) has to be increased for both approaches. To maximize the signal measured in a given time, it should be chosen such that $2\tau \approx T_{2,\mathrm{NV}}$, as this ensures a high DEER intensity [$T \approx \tau$ in Eq. (2)] while preserving enough NV echo contrast and thus a sufficient signal-to-noise ratio. Since we expect typically a longer $T_{2,\mathrm{NV}}$ in diamonds with lower nitrogen content, matching the $2\tau \approx T_{2,\mathrm{NV}}$ condition will result in a sensitivity improvement for DEER partially compensating the overall lower density of bath spins to be detected. Additionally, dynamical decoupling sequences [48] could enhance $T_{2,\mathrm{NV}}$ even further and, as a consequence, the DEER techniques presented in this paper are not restricted to the nitrogen concentrations of sample A and B, 13 and 17 ppm respectively, and can be therefore applied to even more dilute N-doped diamond layers of in principle any thickness. It can be hypothesized that nitrogen is present in the sample in form other than N_s^0, NVH$^-$ or NV$^-$, as the charged N_s^+, which has been reported to be present in CVD crystals, e.g., by Edmonds *et al.* [20]. However, N_s^+ is nonparamagnetic thus cannot be detected in DEER, and the infrared absorption technique used by Edmonds *et al.* to quantify N_s^+ lacks the sensitivity for reliable estimation in our submicron thick layers.

In conclusion, we have shown that optically detected DEER with NV$^-$ centers can be applied for detecting and investigating NVH$^-$ centers in submicron-thick diamond layers. Since the method relies on NV$^-$ centers as local magnetic field sensors, optically detected DEER is decoupled from the sample volume and works, therefore, even on the nanoscale. The ability to estimate the concentration of NVH$^-$ in the range of a few hundreds of ppb, opens the possibility to compare and engineer spin bath environments aiming for higher N-to-NV conversion ratios without the need for thick bulk samples. This might boost the understanding of the defect generation during CVD diamond growth and pave the way for better diamond material for quantum applications. Furthermore, being sensitive not only to N_s^0 but also NVH$^-$, optically detected DEER could be employed for imaging dark spins using a wide-field microscope offering entirely new insights into defect correlation and material heterogeneity on the mesoscale.

ACKNOWLEDGMENTS

The authors thank P. Vetter for experimental support and acknowledge also the support by Cambridge Isotope Laboratories Inc. This work was funded by "European Research Council" (HyperQ GAno. 856432), "Bundesministerium für Bildung und Forschung" Germany (QSCALE Fkz. 03ZU1110GB, QSPACE Fkz. 03ZU1110JA), and "Ministerium für Wirtschaft, Arbeit und Tourismus Baden-Württemberg" (QC-4BW Az. 3-4332.62-IAF/7, QC-4BW-2 Az. WM3-4332-96/10).

[1] D. J. Christle, A. L. Falk, P. Andrich, P. V. Klimov, J. U. Hassan, N. T. Son, E. Janzén, T. Ohshima, and D. D. Awschalom, Isolated electron spins in silicon carbide with millisecond coherence times, Nat. Mater. **14**, 160 (2015).

[2] G. Balasubramanian, P. Neumann, D. Twitchen, M. Markham, R. Kolesov, N. Mizuochi, J. Isoya, J. Achard, J. Beck, J. Tissler *et al.*, Ultralong spin coherence time in isotopically engineered diamond, Nat. Mater. **8**, 383 (2009).

[3] D. D. Awschalom, R. Hanson, J. Wrachtrup, and B. B. Zhou, Quantum technologies with optically interfaced solid-state spins, Nat. Photo. **12**, 516 (2018).

[4] F. Jelezko and J. Wrachtrup, Read-out of single spins by optical spectroscopy, J. Phys.: Condens. Matter **16**, R1089 (2004).

[5] E. D. Herbschleb, H. Kato, Y. Maruyama, T. Danjo, T. Makino, S. Yamasaki, I. Ohki, K. Hayashi, H. Morishita, M. Fujiwara, and N. Mizuochi, Ultra-long coherence times amongst room-temperature solid-state spins, Nat. Commun. **10**, 3766 (2019).

[6] S. Schmitt, T. Gefen, F. M. Stürner, T. Unden, G. Wolff, C. Müller, J. Scheuer, B. Naydenov, M. Markham, S. Pezzagna *et al.*, Submillihertz magnetic spectroscopy performed with a nanoscale quantum sensor, Science **356**, 832 (2017).

[7] P. J. Vetter, A. Marshall, G. T. Genov, T. F. Weiss, N. Striegler, E. F. Großmann, S. Oviedo-Casado, J. Cerrillo, J. Prior, P. Neumann, and F. Jelezko, Zero- and low-field sensing with nitrogen-vacancy centers, Phys. Rev. Appl. **17**, 044028 (2022).

[8] T. Staudacher, F. Shi, S. Pezzagna, J. Meijer, J. Du, C. A. Meriles, F. Reinhard, and J. Wrachtrup, Nuclear magnetic resonance spectroscopy on a (5-nanometer)^3 sample volume, Science **339**, 561 (2013).

[9] N. Staudenmaier, A. Vijayakumar-Sreeja, S. Oviedo-Casado, G. Genov, D. Cohen, D. Dulog, T. Unden, N. Striegler, A. Marshall, J. Scheuer *et al.*, Power-law scaling of correlations in statistically polarised nano-NMR, npj Quantum Inf. **8**, 120 (2022).

[10] K. S. Liu, X. Ma, R. Rizzato, A. L. Semrau, A. Henning, I. D. Sharp, R. A. Fischer, and D. B. Bucher, Using metal–organic frameworks to confine liquid samples for nanoscale NV-NMR, Nano Lett. **22**, 9876 (2022).

[11] D. R. Glenn, D. B. Bucher, J. Lee, M. D. Lukin, H. Park, and R. L. Walsworth, High-resolution magnetic resonance spectroscopy using a solid-state spin sensor, Nature (London) **555**, 351 (2018).

[12] D. B. Bucher, D. R. Glenn, H. Park, M. D. Lukin, and R. L. Walsworth, Hyperpolarization-enhanced NMR spectroscopy with femtomole sensitivity using quantum defects in diamond, Phys. Rev. X **10**, 021053 (2020).

[13] V. Stepanov and S. Takahashi, Determination of nitrogen spin concentration in diamond using double electron-electron resonance, Phys. Rev. B **94**, 024421 (2016).

[14] A. M. Edmonds, U. F. S. D'Haenens-Johansson, R. J. Cruddace, M. E. Newton, K.-M. C. Fu, C. Santori, R. G. Beausoleil, D. J. Twitchen, and M. L. Markham, Production of oriented nitrogen-vacancy color centers in synthetic diamond, Phys. Rev. B **86**, 035201 (2012).

[15] K. Ohno, F. Joseph Heremans, L. C. Bassett, B. A. Myers, D. M. Toyli, A. C. Bleszynski Jayich, C. J. Palmstrøm, and D. D. Awschalom, Engineering shallow spins in diamond with nitrogen delta-doping, Appl. Phys. Lett. **101**, 082413 (2012).

[16] T. R. Eichhorn, C. A. McLellan, and A. C. Bleszynski Jayich, Optimizing the formation of depth-confined nitrogen vacancy center spin ensembles in diamond for quantum sensing, Phys. Rev. Mater. **3**, 113802 (2019).

[17] C. Osterkamp, J. Lang, J. Scharpf, C. Müller, L. P. McGuinness, T. Diemant, R. J. Behm, B. Naydenov, and F. Jelezko, Stabilizing shallow color centers in diamond created by nitrogen delta-doping using SF_6 plasma treatment, Appl. Phys. Lett. **106**, 113109 (2015).

[18] M. A. Lobaev, A. M. Gorbachev, S. A. Bogdanov, A. L. Vikharev, D. B. Radishev, V. A. Isaev, V. V. Chernov, and M. N. Drozdov, Influence of CVD diamond growth conditions on nitrogen incorporation, Diam. Relat. Mater. **72**, 1 (2017).

[19] C. Osterkamp, P. Balasubramanian, G. Wolff, T. Teraji, M. Nesladek, and F. Jelezko, Benchmark for synthesized diamond sensors based on isotopically engineered nitrogen–vacancy spin ensembles for magnetometry applications, Adv. Quantum Technol. **3**, 2000074 (2020).

[20] A. M. Edmonds, C. A. Hart, M. J. Turner, P.-O. Colard, J. M. Schloss, K. S. Olsson, R. Trubko, M. L. Markham, A. Rathmill, B. Horne-Smith *et al.*, Characterisation of CVD diamond with high concentrations of nitrogen for magnetic-field sensing applications, Mater. Quantum. Technol. **1**, 025001 (2021).

[21] A. Tallaire, O. Brinza, P. Huillery, T. Delord, C. Pellet-Mary, R. Staacke, B. Abel, S. Pezzagna, J. Meijer, N. Touati *et al.*, High NV density in a pink CVD diamond grown with N_2O addition, Carbon **170**, 421 (2020).

[22] P. Balasubramanian, C. Osterkamp, O. Brinza, M. Rollo, I. Robert-Philip, P. Goldner, V. Jacques, F. Jelezko, J. Achard, and A. Tallaire, Enhancement of the creation yield of NV ensembles in a chemically vapour deposited diamond, Carbon **194**, 282 (2022).

[23] A. Cox, M. E. Newton, and J. M. Baker, ^{13}C, ^{14}N and ^{15}N ENDOR measurements on the single substitutional nitrogen centre (P1) in diamond, J. Phys.: Condens. Matter **6**, 551 (1994).

[24] E. Bauch, S. Singh, J. Lee, C. A. Hart, J. M. Schloss, M. J. Turner, J. F. Barry, L. M. Pham, N. Bar-Gill, S. F. Yelin, and R. L. Walsworth, Decoherence of ensembles of nitrogen-vacancy centers in diamond, Phys. Rev. B **102**, 134210 (2020).

[25] L. Rondin, J.-P. Tetienne, T. Hingant, J.-F. Roch, P. Maletinsky, and V. Jacques, Magnetometry with nitrogen-vacancy defects in diamond, Rep. Prog. Phys. **77**, 056503 (2014).

[26] T. Luo, L. Lindner, J. Langer, V. Cimalla, X. Vidal, F. Hahl, C. Schreyvogel, S. Onoda, S. Ishii, T. Ohshima *et al.*, Creation of nitrogen-vacancy centers in chemical vapor deposition diamond for sensing applications, New J. Phys. **24**, 033030 (2022).

[27] S. Chouaieb, L. J. Martínez, W. Akhtar, I. Robert-Philip, A. Dréau, O. Brinza, J. Achard, A. Tallaire, and V. Jacques, Optimizing synthetic diamond samples for quantum sensing technologies by tuning the growth temperature, Diam. Relat. Mater. **96**, 85 (2019).

[28] C. Glover, M. E. Newton, P. Martineau, D. J. Twitchen, and J. M. Baker, Hydrogen incorporation in diamond: The nitrogen-vacancy-hydrogen complex, Phys. Rev. Lett. **90**, 185507 (2003).

[29] J. P. Goss, P. R. Briddon, R. Jones, and S. Sque, The vacancy–nitrogen–hydrogen complex in diamond: A potential deep centre in chemical vapour deposited material, J. Phys.: Condens. Matter **15**, S2903 (2003).

[30] A. Stacey, T. J. Karle, L. P. McGuinness, B. C. Gibson, K. Ganesan, S. Tomljenovic-Hanic, A. D. Greentree, A. Hoffman,

R. G. Beausoleil, and S. Prawer, Depletion of nitrogen–vacancy color centers in diamond via hydrogen passivation, Appl. Phys. Lett. **100**, 071902 (2012).

[31] C. Findler, J. Lang, C. Osterkamp, M. Nesládek, and F. Jelezko, Indirect overgrowth as a synthesis route for superior diamond nano sensors, Sci. Rep. **10**, 22404 (2020).

[32] G. R. Eaton, S. S. Eaton, D. P. Barr, and R. T. Weber, *Quantitative EPR* (Springer, Wien, 2010).

[33] J. N. Lomer and A. M. A. Wild, Electron spin resonance in electron irradiated diamond annealed to high temperatures, Radiat. Eff. **17**, 37 (1973).

[34] D. J. Twitchen, M. E. Newton, J. M. Baker, T. R. Anthony, and W. F. Banholzer, An annealing study of the R1 EPR centre (the nearest-neighbour di-⟨100⟩-split self-interstitial) in diamond, J. Phys.: Condens. Matter **13**, 2045 (2001).

[35] T. Yamamoto, T. Umeda, K. Watanabe, S. Onoda, M. L. Markham, D. J. Twitchen, B. Naydenov, L. P. McGuinness, T. Teraji, S. Koizumi, F. Dolde, H. Fedder, J. Honert, J. Wrachtrup, T. Ohshima, F. Jelezko, and J. Isoya, Extending spin coherence times of diamond qubits by high-temperature annealing, Phys. Rev. B **88**, 075206 (2013).

[36] L. M. Pham, D. Le Sage, P. L. Stanwix, T. K. Yeung, D. Glenn, A. Trifonov, P. Cappellaro, P. R. Hemmer, M. D. Lukin, H. Park *et al.*, Magnetic field imaging with nitrogen-vacancy ensembles, New J. Phys. **13**, 045021 (2011).

[37] D. R. Glenn, K. Lee, H. Park, R. Weissleder, A. Yacoby, M. D. Lukin, H. Lee, R. L. Walsworth, and C. B. Connolly, Single-cell magnetic imaging using a quantum diamond microscope, Nat. Methods **12**, 736 (2015).

[38] D. A. Simpson, J.-P. Tetienne, J. M. McCoey, K. Ganesan, L. T. Hall, S. Petrou, R. E. Scholten, and L. C. L. Hollenberg, Magneto-optical imaging of thin magnetic films using spins in diamond, Sci. Rep. **6**, 22797 (2016).

[39] J.-P. Tetienne, N. Dontschuk, D. A. Broadway, A. Stacey, D. A. Simpson, and L. C. L. Hollenberg, Quantum imaging of current flow in graphene, Sci. Adv. **3**, e1602429 (2017).

[40] A. J. Healey, A. Stacey, B. C. Johnson, D. A. Broadway, T. Teraji, D. A. Simpson, J.-P. Tetienne, and L. C. L. Hollenberg, Comparison of different methods of nitrogen-vacancy layer formation in diamond for wide-field quantum microscopy, Phys. Rev. Mater. **4**, 104605 (2020).

[41] T. Luo, L. Lindner, R. Blinder, M. Capelli, J. Langer, V. Cimalla, F. A. Hahl, X. Vidal, and J. Jeske, Rapid determination of single substitutional nitrogen N_s concentration in diamond from UV-Vis spectroscopy, Appl. Phys. Lett. **121**, 064002 (2022).

[42] M. J. Degen, S. J. H. Loenen, H. P. Bartling, C. E. Bradley, A. L. Meinsma, M. Markham, D. J. Twitchen, and T. H. Taminiau, Entanglement of dark electron-nuclear spin defects in diamond, Nat. Commun. **12**, 3470 (2021).

[43] S. Li, H. Zheng, Z. Peng, M. Kamiya, T. Niki, V. Stepanov, A. Jarmola, Y. Shimizu, S. Takahashi, A. Wickenbrock, and D. Budker, Determination of local defect density in diamond by double electron-electron resonance, Phys. Rev. B **104**, 094307 (2021).

[44] See Supplemental Material at http://link.aps.org/supplemental/10.1103/PhysRevMaterials.8.026203 for the description of the numerical evaluation of the pulse propagator to quantitatively fit DEER spectra with multiple spectrally overlapping spin species. A summary of all fit parameters is also provided including the DEER spectra and pi shift method for ^{14}NVH, see Secs. 1.1, 1.3, 1.5.1, 1.5.2, Figs. S6, S7, S9, S10, and Tables S5–S8.

[45] C. Osterkamp, M. Mangold, J. Lang, P. Balasubramanian, T. Teraji, B. Naydenov, and F. Jelezko, Engineering preferentially-aligned nitrogen-vacancy centre ensembles in CVD grown diamond, Sci. Rep. **9**, 5786 (2019).

[46] S. Stoll and A. Schweiger, EasySpin, a comprehensive software package for spectral simulation and analysis in EPR, J. Magn. Reson. **178**, 42 (2006).

[47] L. B. Hughes, Z. Zhang, C. Jin, S. A. Meynell, B. Ye, W. Wu, Z. Wang, E. J. Davis, T. E. Mates, N. Y. Yao, K. Mukherjee, and A. C. B. Jayich, Two-dimensional spin systems in PECVD-grown diamond with tunable density and long coherence for enhanced quantum sensing and simulation, APL Mater. **11**, 021101 (2023).

[48] G. A. Álvarez, A. Ajoy, X. Peng, and D. Suter, Performance comparison of dynamical decoupling sequences for a qubit in a rapidly fluctuating spin bath, Phys. Rev. A **82**, 042306 (2010).